# Multiscale Design and Multiobjective Optimization of Orthopedic Hip Implants with Functionally Graded Cellular Material

**Sajad Arabnejad Khanoki**
Ph.D. Student
e-mail: sajad.arabnejadkhanoki@mail.mcgill.ca

**Damiano Pasini**[1]
Associate Professor
e-mail: Damiano.pasini@mcgill.ca

Mechanical Engineering Department,
McGill University,
Montreal, Quebec, Canada, H3A 0C3

*Revision surgeries of total hip arthroplasty are often caused by a deficient structural compatibility of the implant. Two main culprits, among others, are bone-implant interface instability and bone resorption. To address these issues, in this paper we propose a novel type of implant, which, in contrast to current hip replacement implants made of either a fully solid or a foam material, consists of a lattice microstructure with nonhomogeneous distribution of material properties. A methodology based on multiscale mechanics and design optimization is introduced to synthesize a graded cellular implant that can minimize concurrently bone resorption and implant interface failure. The procedure is applied to the design of a 2D left implanted femur with optimized gradients of relative density. To assess the manufacturability of the graded cellular microstructure, a proof-of-concept is fabricated by using rapid prototyping. The results from the analysis are used to compare the optimized cellular implant with a fully dense titanium implant and a homogeneous foam implant with a relative density of 50%. The bone resorption and the maximum value of interface stress of the cellular implant are found to be over 70% and 50% less than the titanium implant while being 53% and 65% less than the foam implant.*
[DOI: 10.1115/1.4006115]

*Keywords: total hip replacement, cellular microstructure, lattice material, finite element method, asymptotic homogenization, multiobjective optimization*

## 1 Bone Replacement Implants

Current orthopedic prostheses are generally made of uniform density, homogenous material, such as 316L stainless steel, cobalt chromium alloys, titanium-based alloys and tantalum. Over the last few decades, the design of orthopedic prostheses has been improved to achieve long-term fixation and easy osseointegration. Although technological advances have made current total hip arthroplasty successful, over 13% of hip prostheses still require revision surgeries as a result of bone resorption and aseptic loosening of the implant [1]. Revision surgery is a much more complex procedure than the first total hip arthroplasty (THA) due to bone degradation around the first implant. Bone degradation compromises bone ability to adequately secure the new implant. Although patient-related factors, such as sickle cell anemia [2], poor bone quality [3], and high body mass index, may predispose the patient to prosthetic failures, mechanical rather than medical factors are major causes of implant failure [4]. Excluding biocompatibility requirements, further three requirements can be identified as indicators of implant success: (i) *implant stability in the short and long term*, (ii) *preservation of bone tissue around the implant from resorption*, *and* (iii) *high wear and corrosion resistance of the articulating surfaces*.

The volumetric amount of wear particle and its clinical consequences have been reduced considerably by the development of extremely wear-resistant polymers [5,6] or the design of metal-on-metal implants [7,8]. Yet, the reduction of bone-implant interface instability and bone resorption in the long term still remains a challenge.

Current orthopedic implants are generally stiffer than the bone adjacent to the prosthesis. Due to its high stiffness, an implant prevents the applied stress from being transferred to the adjacent bone, thereby resulting in bone resorption around the implant. This weakens the implant support, which leads to bone fracture and implant loosening. Over the last three decades, alternative implant designs have been proposed to reduce stress shielding and minimize the associated clinical consequences [9]. Recent implant designs have only been partially successful, as the solution of one problem has given rise to another one. For example, to overcome the mismatch between a stiff stem and the adjacent bone, composite and isoelastic hip stems were introduced [10,11]. The results of these studies show an undesired increase of the shear stress between the implant and the bone, an outcome that increases the risk of interface motion [12,13]. These attempts help elucidate the antagonist nature of stress shielding and bone-implant interface stability.

In their seminal work, Kuiper and Huiskes identified the conflict existing between stress shielding and interface shear stress [14,15] and attempted to find a trade-off design for a bi-dimensional hip implant. They showed that one solution to this issue is an implant whose material properties vary locally throughout the structure. A non-homogeneous distribution of elastic properties within the hip stem could contribute to minimizing the probability of interface failure while concurrently limiting the amount of bone loss. In their approach, however, the solution of the multiobjective problem was simplified, reformulated and solved as a single objective optimization problem. As a result, the whole set of

[1]Corresponding author. Room 372, MacDonald Engineering Building, Mechanical Engineering Department, McGill University, Montreal, Quebec, Canada, H3A 0C3.

Contributed by the Bioengineering Division of ASME for publication in the JOURNAL OF BIOMECHANICAL ENGINEERING. Manuscript received August 30, 2011; final manuscript received February 10, 2012; accepted manuscript posted February 21, 2012; published online March 21, 2012. Assoc. Editor: Stephen Klisch.

  

trade-off designs could not have been captured. Hedia et al. [16,17] attempted to reconcile the conflicting nature of these objective functions by proposing the use of three bioactive materials: hydroxyapatite, Bioglass, and collagen, to design a graded cementless hip stem. Although their implant design reduced bone resorption and bone-implant interface stresses, the use of such bioactive materials have limitations due to their brittleness and insufficient strength when applied to load-bearing applications [18–20]. In a more recent study, Fraldi et al. [21] applied a maximum stiffness topological optimization strategy to re-design a hip prostheses with the goal of reducing stress shielding in the femur. According to this method, elements with intermediate volume fraction (between 0 and 1) are penalized to limit their presence in the final solution. For regions with intermediate relative density, certain microstructures should be proposed to match those materials in terms of effective elastic properties. Laser micro-drilling is suggested to create the required micro-porosity, an option that can be used only on the implant surface, not throughout the implant.

Other advances in total hip replacement have used a microstructured material over a fully dense material. Hip implants with porous tantalum have been proposed in knee and hip replacement surgery [22]. Tantalum foam is an excellent material due to its biocompatibility, high volumetric porosity, and modulus of elasticity similar to that of bone. To create the tantalum foam, pure tantalum is chemically deposited on a carbon skeleton. As a result, the microstructure of a tantalum foam implant has an almost uniform and random distribution of pore shape and size [23] throughout the implant. These material characteristics, however, have been demonstrated to be incapable of solving the conflicting nature of the physiological phenomena occurring in an implant [14,15]. Indeed, whereas the reduced stiffness of the foam decreases bone resorption, the uniform distribution of cells has the undesired effect of increasing the interface stresses.

Recent advances in additive manufacturing, such as Electron-Beam Melting (EBM), Selective Laser Melting (SLM), Stereolithography Apparatus (SLA), and other rapid prototyping techniques, offer the possibility of novel bone-replacement implants with a controlled cellular microstructure [24–28]. As a result, cellular components with tailored microstructures can be built with a high level of quality, accuracy and reliability. Besides providing an exceptional degree of control over the mechanical properties, such manufacturing processes are capable of building graded cellular structures. As demonstrated by the work of Kuiper and Huiskes [14,15], this feature is an asset for bone-replacement implants since the internal skeleton of the prosthesis can be designed to ease osseointegration as well as to match the local mechanical properties of the femoral bone. By properly selecting topology, size, and relative density of the unit cell of the implant, it is thus possible to: (a) fabricate implants which can provide mechanical properties mimicking those of the host bone, (b) manufacture three-dimensional structures with an interconnected porosity and pore sizes suitable to bone ingrowth and vascularization, and (c) customize implants for each patient by using CT scan data of the patient's bone.

While the aforementioned research is promising for the support of cellular microstructure based bone-replacement implants, the literature is limited to the manufacturing aspects or the mechanical testing of biomedical implants with periodic cellular microstructure [24–28]. No study has been found which deals with the multiscale mechanics aspects of an implant with a functionally graded cellular material as well as the multiobjective nature of the features that their design requires.

This paper proposes a systematic methodology for the design of bone-replacement implants with improved structural stability. For total hip arthroplasty, we propose to design an implant with tailored gradients of lattice material that can simultaneously minimize bone resorption and bone-implant interface stress. The procedure that hinges on multiscale mechanics theory and multiobjective optimization is applied to the design of a bi-dimensional femoral hip implant with optimal graded cellular microstructure. Its biocompatibility performance is discussed with respect to that of currently-used hip implants.

We note that in this work the terms "cellular," "cell," and "wall cell," refer exclusively to the artificial porous material of the implant. These terms neither refer to body cells nor have a biological or medical connotation.

## 2 Methodology

Kuiper and Huiskes [14,15] showed that the use of a graded material in an orthopedic stem can lead to a reduction of both stress shielding and bone-implant interface stress. To this end, hierarchical computational procedures [29–32] can be implemented to design an optimum material distribution within the implant. These strategies might generally require a high computational cost besides yielding a microstructure which is difficult to fabricate. In this work, we suggest to design gradients of material properties through a tailored lattice microstructure, whose geometrical parameters are optimized in each region of the implant to achieve minimum bone loss and implant interface failure.

The mechanical properties of a cellular structure depend on the relative density and the geometric parameters of the unit cell, as described, for example, by the expression of the Young's modulus [33]:

$$E^* = CE_s\left(\frac{\rho}{\rho_s}\right)^m \tag{1}$$

where $E^*$ is the effective Young's modulus of the unit cell, $\rho$ is the density of the unit cell, and $E_s$ and $\rho_s$ are the Young's modulus and density of the constitutive material, respectively. In addition, $m$ has a value varying from 1 to 3, as determined by the mechanical failure mode of the unit cell, and $C$ is a geometric constant of the unit cell. By changing the relative density of the lattice microstructure, it is thus possible to obtain desired values of mechanical properties in any zone of the implant.

Figure 1 summarizes the procedure proposed here to design a cellular implant with controlled gradients of mechanical properties. The method integrates a multiscale mechanics approach to deal with the scale-dependent material structure and a multiobjective optimization strategy to handle the conflicting nature of bone resorption and implant interface failure. The main steps identified by the numbers reported in the flow chart of Fig. 1 are described here:

- (1-2) A finite element model of the bone is created by processing CT-scan data of a patient bone. The design domain of the prosthesis is assumed to possess a 3D lattice microstructure, where the unit cell, i.e., the building block, can be of any arbitrary topology (Fig. 1). The microscopic parameters of the unit cell geometry and the macroscopic shape of the implant are the design variables of the vector $\boldsymbol{b}$. The unit cell is assumed to be locally periodic, and its field quantities, such as stress and strain, to vary smoothly through the implant.
- (3) The characteristic length of the unit cell in the cellular implant is assumed to be much smaller than the characteristic length of the macrodimensions of the implant. Hence, the microstructure can be replaced with a homogeneous medium whose equivalent mechanical properties, in particular the homogenized stiffness tensor of each unit cell, are calculated through asymptotic homogenization theory [34–38].
- (4,5) The homogenized stiffness tensors are then used to construct the stiffness matrix which will be the input to the Finite Element (FE) solver. As a result, the average strains and stresses throughout the bone and the structure of the prosthesis are calculated.
- (6) To obtain the microscopic stress field for each unit cell from the macroscopic strain, the stress recovery procedure illustrated in Refs. [34,38–40] is used.
- (7) If the microscopic stress level is below a predefined failure criterion, the macroscopic stresses and strains

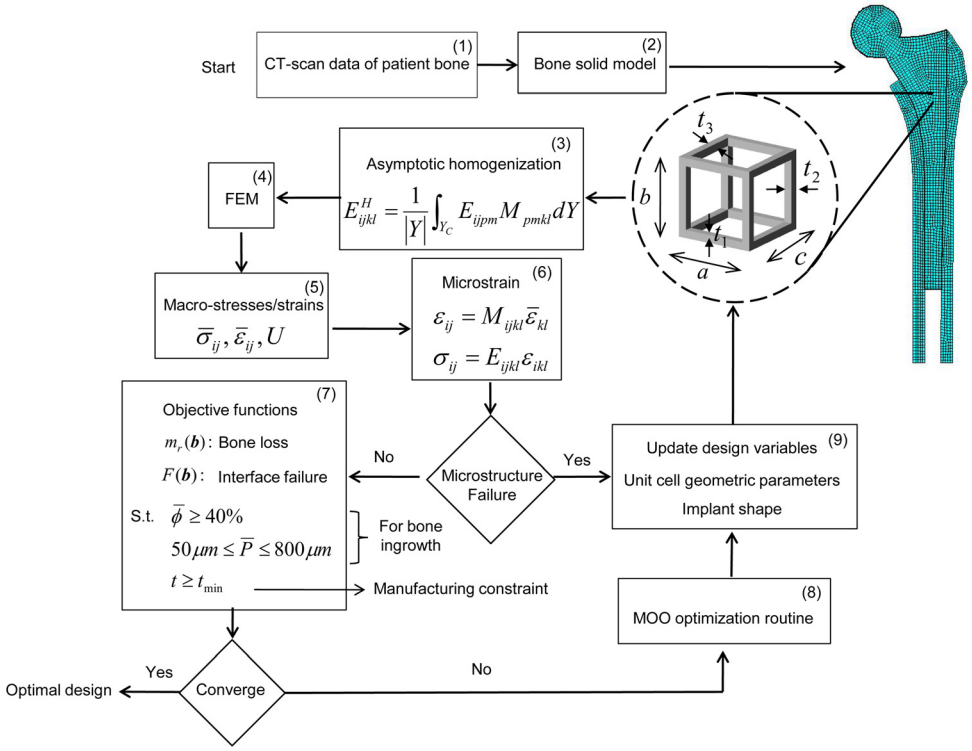


**Fig. 1 Flow chart illustrating the design of a graded cellular hip implant minimizing bone resorption and implant interface failure**

representing the mechanical behavior of the implant are used to evaluate bone loss ($m_r(\boldsymbol{b})$) and interface failure ($F(\boldsymbol{b})$). In the formulation of the multiobjective optimization problem, the constraints are set on the average porosity of the cellular implant $\bar{\phi}(\boldsymbol{b})$, the mean pore size $\bar{P}$, and the minimum thickness of cell walls $t_{\min}$. In particular, $\bar{\phi}(\boldsymbol{b}) \geq 40\%$ and 50 $\mu$m $\leq \bar{P} \leq$ 800 $\mu$m are selected to ease bone ingrowth [41,42]. The thickness of the cell walls is selected to be greater than the minimum resolution $t_{\min}$ offered by a given manufacturing process. For example, $t_{\min}$ is 100 $\mu$m and 70 $\mu$m, respectively, for SLM and SLA [27,43].

- (8-9) If the solutions of the optimization have not converged, then the vector $b$ of the design variables are updated to find the set of non-dominated solutions of the Pareto front.
- (9) If the unit cell fails at the microscale level, the cell walls will be iteratively increased to reduce the microscopic stresses.

As described above, multiscale mechanics and multiobjective optimization are integrated aspects of the method proposed in this paper. Their descriptions are separately detailed in the following subsections.

**2.1 Multiscale Analysis and Design of a Cellular Implant.** The deformation and failure mechanisms of a structure with heterogeneous material can occur at both the macroscopic and microscopic scales. In a full scale simulation, the heterogeneities are explicitly modeled at the microscale to guarantee high accuracy. The computational effort, however, can be very lengthy and time-consuming. As an alternative, the microstructure can be replaced by a homogeneous medium, and the mathematical theory of homogenization can be used to characterize the mechanical behavior of heterogeneous media [44]. As shown in Fig. 2, a body $\Omega^\varepsilon$ with a periodic microstructure subjected to the traction $t$ at the traction boundary $\Gamma_t$, a displacement $d$ at the displacement boundary $\Gamma_d$, and a body force $f$ can be replaced by a homogenized body $\Omega$ with the prescribed external and traction boundaries applied to $\Omega^\varepsilon$, without geometrical details and voids of the local coordinate system.

The homogenized properties and strength of a cellular structure can be obtained by performing either analytical or numerical or experimental approaches [33–39,45–53]. Extensive efforts have been devoted to the derivation of the equivalent mechanical properties

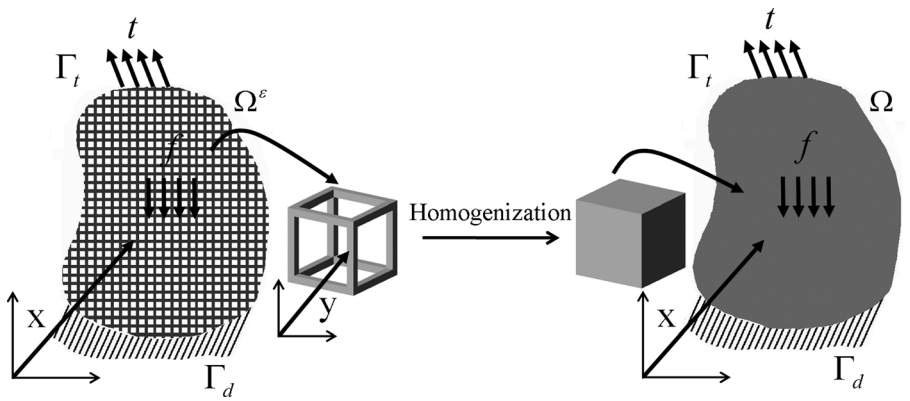


**Fig. 2 Homogenization concept of a cellular structure**

by structural analysis [33,45–50]. In these studies, the effective moduli and yield strength of a cellular material are generally modeled by assuming that the cell walls flex like beams. Despite the simplicity of this method in calculating the overall mechanical properties, the results are reliable only if the relative density is lower than 0.3 [47]. Furthermore, the actual stress distribution within the unit cell walls cannot be captured. As an alternative method, the asymptotic homogenization method is used in this work to deal with the multiscale analysis of the cellular implant. This technique is applied to calculate the homogeneous stiffness matrix of the unit cell for different values of relative density as well as to determine the microscopic stresses and strains [34,38,39]. The asymptotic homogenization method has been widely used in topology optimization [34,54–58] and hierarchical design of materials and structures [29–32]. In this work, unlike hierarchical topology optimization, a predefined unit cell topology with parametric geometry is considered as the microstructure of the implant; then, the optimization algorithm searches for the optimum unit cell geometry of the lattice to minimize the antagonist objective functions under a set of constraints. This procedure is similar to the one developed by Bendsøe and Kikuchi [58] and is not limited to any cell topology; we selected the hollow square cell as an example to demonstrate the methodology. A brief explanation about the asymptotic homogenization technique and the main steps to calculate the effective stiffness and microscopic stress and strain are provided below.

The approach assumes that each field quantity depends on two different scales: one on the macroscopic level x, and the other on the microscopic level, $y = x/\varepsilon$, where $\varepsilon$ is a magnification factor that enlarges the dimensions of a unit cell to make it comparable with the dimensions of the material. The field quantities, such as displacement, stress, and strain, are assumed to vary smoothly at the macroscopic level, being periodic at the microscale [35–39]. The effective properties of the periodic material are determined through the solution of local problems formulated on the representative volume element (RVE) of the material. As a result, the homogenized stiffness tensor ($E^H_{ijkl}$) of a cellular material may be defined as follow [39]:

$$E^H_{ijkl} = \frac{1}{|Y|}\int_{Y_C} E_{ijpm} M_{pmkl} dY \tag{2}$$

where $|Y|$ is the volume of the entire unit cell with void, $Y_c$ is the solid part of the cell, $E_{ijkl}$ is the local elasticity tensor that depends on the position within the representative volume element, i.e., $E_{ijkl}$ is equal to the elasticity tensor of the material located in the cell walls and it vanishes in the voids. $M_{ijkl}$ is the local structure tensor, which relates the macroscopic strains ($\bar{\varepsilon}$) to the local or microstructural strains ($\varepsilon$) through the relation:

$$\varepsilon_{ij} = M_{ijkl}\bar{\varepsilon}_{kl} \tag{3a}$$

$$M_{ijkl} = \frac{1}{2}(\delta_{ik}\delta_{jl} + \delta_{il}\delta_{jk}) - \varepsilon^{*kl}_{ij} \tag{3b}$$

where $\delta_{ij}$ is the Kronecker $\zeta$, and $\varepsilon^{*kl}_{ij}$ is the microstructural strain corresponding to the component $kl$ of the macroscopic strain tensor ($\bar{\varepsilon}_{kl}$). $\varepsilon^{*kl}_{ij}$ is the solution of the following equation:

$$\int_{Y_C} E_{ijpm}\varepsilon^1_{ij}(v)\varepsilon^{*kl}_{pm}(u)dY = \int_{Y_C} E_{ijkl}\varepsilon^1_{ij}(v)\bar{\varepsilon}_{kl}dY \tag{4}$$

where $\varepsilon^1_{ij}(v)$ is the virtual strain. In general, $\bar{\varepsilon}_{kl}$ can be an arbitrary macroscopic strain tensor. Considering the assumption of small deformation and linear material behavior, $\bar{\varepsilon}_{kl}$ may be written as a linear combination of unit strains. For a two-dimensional case, the unit strains are defined as:

$$\bar{\varepsilon}_{11} = [1 \quad 0 \quad 0]^T, \quad \bar{\varepsilon}_{22} = [0 \quad 1 \quad 0]^T, \quad \bar{\varepsilon}_{12} = [0 \quad 0 \quad 1]^T \tag{5}$$

To calculate the effective mechanical properties of a cellular material, the first task is to obtain the matrix $M_{ijkl}$. After discretizing the RVE domain, the unit strains are applied to each element of the FE model. Periodicity of the strain field is ensured by imposing periodic boundary conditions on the RVE edges. The direct method [59] is selected here to derive periodic boundary conditions. The microscopic strain field ($\varepsilon^{*kl}_{ij}$) inside the RVE is obtained by solving Eq. (4). The results are substituted into Eq. (3*b*) to calculate the local structure tensor $M_{ijkl}$ for each element of the RVE. Finally, the effective stiffness tensor $E^H_{ijkl}$ is obtained by calculating Eq. (2). Once the local structure tensor, $M_{ijkl}$, is obtained, the microscopic strains and stresses corresponding to the macroscopic strain can be obtained via Eq. (3*a*) and the constitutive equation of the cell wall material.

The steps described above are used to compute the homogenized stiffness tensor for each unit cell of the cellular hip implant (Fig. 1). These tensors are used to construct the global stiffness matrix for the FE solver to obtain macroscopic stress and strain distribution within bone and implant. The values are then postprocessed to evaluate the objective functions of the multiobjective optimization problem, whose formulation is described in the following section.

**2.2 Formulation of the Multiobjective Optimization Problem.** For the design of an optimum implant, we impose the simultaneous minimization of the amount of bone loss around the prosthesis, and the probability of mechanical failure at the bone-implant interface. As illustrated in Fig. 1, the multiobjective optimization problem can be formulated as:

$$\begin{aligned} &\text{Minimize}: \begin{cases} m_r(\boldsymbol{b}) & \text{bone loss} \\ F(\boldsymbol{b}) & \text{interface failure} \end{cases} \\ &\text{Subject to} \quad \begin{aligned} &\bar{\phi}(\boldsymbol{b}) \geq 40\% && \text{average porosity} \\ &50\mu\text{m} \leq \bar{P} \leq 800\mu\text{m} && \text{meanpore size} \\ &t \geq t_{\min} && \text{cell wall thickness} \end{aligned} \end{aligned} \tag{6}$$

The amount of bone loss around the stem is determined by assessing the amount of bone that is underloaded. Bone can be considered locally underloaded when its local strain energy ($U_i$) per unit of bone mass ($\rho$), averaged over $n$ loading cases ($S = \frac{1}{n}\sum_{i=1}^{n}\frac{U_i}{\rho}$), is beneath the local reference value $S_{ref}$, which is the value of $S$ when no prosthesis is present. However, it has been observed that not all the underloading leads to resorption; rather a certain fraction of underloading (the threshold level or dead zone s) is tolerated. In fact, bone resorption starts when the local value of $S$ is beneath the value of $(1-s)S_{ref}$ [14,60]. Using this definition, the resorbed bone mass fraction $m_r$ can be obtained from:

$$m_r(\boldsymbol{b}) = \frac{1}{M}\int_V g(S(\boldsymbol{b}))\rho dV \tag{7}$$

where $M$ and $V$ are the original bone mass and volume respectively, and $g(S(\boldsymbol{b}))$ is a resorptive function equal to unity if the local value of $S$ is beneath the local value of $(1-s)S_{ref}$ and equal to 0 if $(1-s)S_{ref} < S$. In this study, the value of the dead zone $s$ is assumed to be 0.5 [14].

The other objective is to minimize the probability of local interface failure, which is expressed by the following functional of the interface stress distribution:

$$F(\boldsymbol{b}) = \frac{1}{n}\sum_{i=1}^{n}\int_{\Pi} f(\sigma^{\text{b}}_i)d\Pi \tag{8}$$

where $F(b)$ is the global interface function index, $\sigma^b_i$ is the interface stress at the loading case i, depending on the design variable $\boldsymbol{b}$, $\Pi$ is the interface area, and $f(\sigma^b_i)$ is the local interface stress function, which is defined based on the multi-axial Hoffman failure criterion [61]. This function is used to determine where local

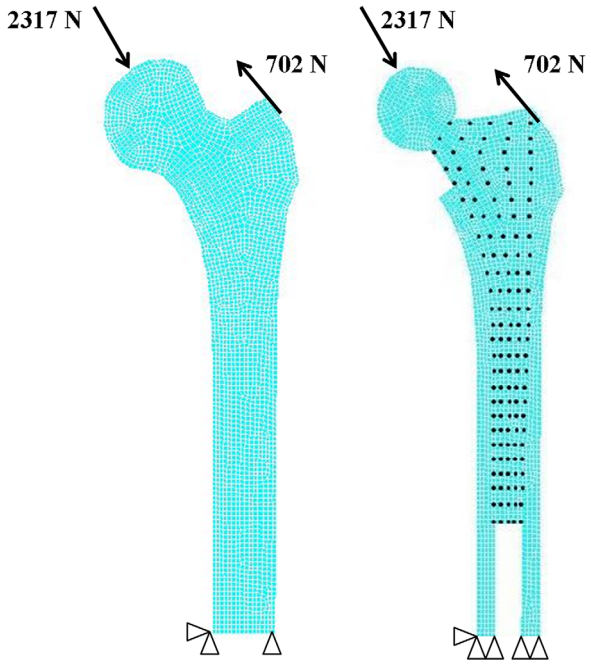


**Fig. 3 2D Finite element models of the femur (left) and the prosthesis implanted into the femur (right)**

debonding might occur along the bone-implant interface [14,62]. The probability of local interface failure $f(\sigma)$ is given by:

$$f(\sigma) = \frac{1}{S_t S_c}\sigma_n^2 + \left(\frac{1}{S_t} - \frac{1}{S_c}\right)\sigma_n + \frac{1}{S_s^2}\tau^2 \tag{9}$$

where $S_t$ and $S_c$ are the uniaxial tensile and compressive strengths, respectively, $S_s$ is the shear strength, and $\sigma_n$ and $\tau$ are normal and shear stresses at the bone-implant interface, respectively. For $f(\sigma) \gg 1$, a high probability of failure is expected, whereas for $f(\sigma) \ll 1$ the risk of interface failure is low. Tensile, compression, and shear strengths of bone can be expressed as a function of bone density, following the power law relations obtained by Pal et al. [62]

$$S_t = 14.5\rho^{1.71}, \quad S_c = 32.4\rho^{1.85}, \quad S_s = 21.6\rho^{1.65} \tag{10}$$

The distribution of bone density can be obtained through a CT-scan data of bone and then used in Eq. (10) to find the effective mechanical properties of the bone, from which the local interface failure can be determined via Eq. (9). Finally, the interface failure index, $F(\boldsymbol{b})$, is evaluated by means of Eq. (8). It should be noted that $F(b)$ serves as a qualitative indicator only; lower values of $F(b)$ indicate reduced probability of local interface failure in the implant.

The expressions of bone resorption after implantation, and mechanical failure of bone-implant interface described in this section are used in the finite element analysis to evaluate the objective functions to be optimized. The following sections shows the application of the method for the design of a two dimensional cellular implant.

## 3 Application of the Methodology to design a 2D Femoral Implant with a Graded Cellular Material

**3.1 FEM model of the Femur at the Macroscale.** The left hand side of Fig. 3 shows the geometry of the left femur considered in this work along with the appropriate loads and boundary conditions. These data have been obtained from the work of Kuiper and Huiskes [14]. The 3D geometry of the femur is simplified into a 2D model where the thickness of the stem and bone varies such that the second moment of area about the out-of-plane axis does not differ in both models [16]. Furthermore, in this paper, the implant material is designed to be an open cell lattice to ease bone in growth in the implanted stem and obtain a full bond. Although bone ingrowth does not exist in a postoperative situation, it can appear later if local mechanical stability is guaranteed. The minimization of interface stress reduces the possibility of occurrence of interface micromotion and instability [4]. Therefore, to decrease the computational cost required by a stability analysis based on a nonlinear frictional contact model, the prosthesis and the surrounding bone are assumed fully bonded.

The load case represents daily static loading during the stance phase of walking [63]. The distal end of the femur is fixed to avoid rigid body motion. For the material properties of the model, we consider 20 GPa as the Young's modulus of the cortical bone and 1.5 GPa for the proximal bone. The Poisson's ratio is set to be 0.3 [14].

**3.2 FEM model of the Cellular Implant at the Microscale.** The right hand side of Fig. 3 illustrates the model of a cementless prosthesis implanted into the human femur. The grid depicts the domain of the implant to be designed with a lattice material of graded properties. Figure 4 shows the unit cell geometry used for the tessellation of the whole implant. The gradients of material properties are governed by the lattice relative density, which is a variable controlled by the cell size and wall thickness of the hollow square. In future work, the performance of alternative cell topologies suitable for bone tissue scaffolding will be investigated, as well as combinations of dissimilar unit cells in the tessellation [64].

For the material property of the implant, we consider Ti6Al4V [24], which is a biocompatible material commonly used in EBM. Its mechanical properties are the following: 900 MPa for the yield strength of the solid material, 120 GPa for Young's modulus, and 0.3 for Poisson's ratio.

**3.3 Design of the Graded Cellular Material of the Implant.** The procedure introduced in this paper for the design of a graded cellular implant requires both multiscale analysis and multiobjective optimization, as described in Secs. 2.1 and 2.2 and shown in Fig. 1. The variables of the lattice model are the relative densities attributed to 130 sampling points, 26 rows along the

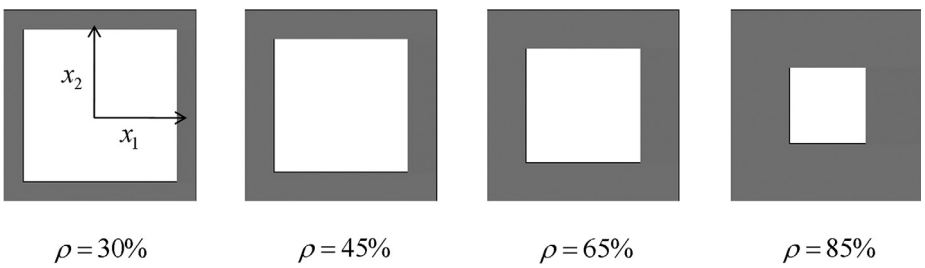


**Fig. 4 2D hollow square unit cell for given values of relative density**

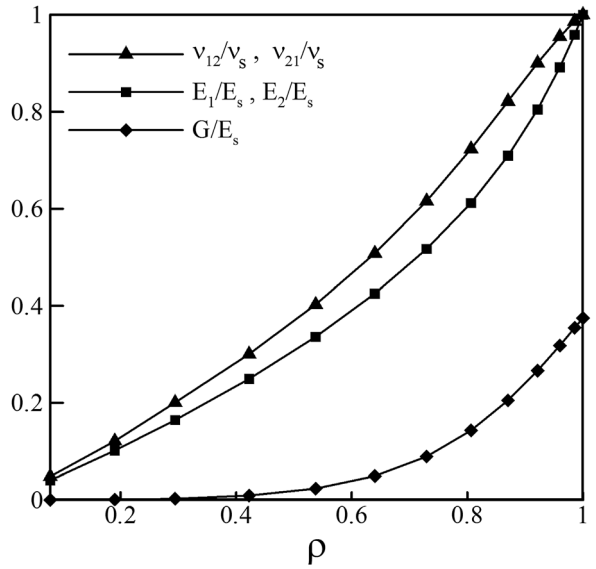


**Fig. 5 Effective Young's modulus of 2D square lattice versus relative density. Solution points obtained through homogenization theory are fitted with the least squares method.**

prosthetic length and 5 columns along the radial direction, as shown in the right side of Fig. 3. The number of sampling points has been chosen to be 130 to limit the computational time required for the analysis and optimization, while providing a reasonable resolution for the relative density distribution. For a more refined density distribution, the number of sample points can be increased. Their values have been constrained in the range $0.1 \leq \rho \leq 1$ [47] to prevent elastic buckling from occurring in the unit cell prior to yielding. The values of the relative density between the sampling points are obtained through linear interpolation. Although not considered in the current research, the shape of the implant could be included in the vector $\boldsymbol{b}$ as a design variable (Fig. 1).

To calculate the stress and strain regime of the implant, the steps explained in Sec. 2.1 are followed. Initial values of relative density are assigned to each element of the FE model, created in ANSYS (Canonsburg, Pennsylvania, U.S.A). The stiffness matrix of each element is calculated through a computational code, 2DHOMOG, developed in-house, which obtains the homogenized stiffness matrix of the square unit cell as a function of relative density. Figure 5 shows the results which are first obtained at discrete points of relative density. To obtain the continuous functions for the properties, we calculate through the least squares method the expressions (Table 1) for two ranges of relative density, i.e., $\rho < 0.3$ and $\rho > 0.3$. These functions enable to assign the values of the stiffness for a given relative density to each of the sample points modeled in the FE solver. We note that the expressions of Young's moduli and Poisson's ratios in the $x_1$ and $x_2$ directions do not change since the cell thickness is uniform.

Once the stress and strain regimes of the cellular material have been calculated, the non-dominated sorting genetic (NSGA-II) algorithm [65] is employed to solve the multiobjective optimization problem, described in Sec. 2.2. The strain energy within the bone and the stress distribution at the bone-implant interface is then calculated and used in Eqs. (7) and (8) to evaluate the objective functions. The initial population is then sorted based on the nondomination front criterion. A population of solutions, called parents, are selected from the current population, based on their rank and crowding distance. Then, genetic operators are applied to the population of parents to create a population of off-springs. Finally, the next population is produced by taking the best solutions from the combined population of parents and off-springs. The optimization continues until the user-defined number of function evaluations reaches 25,000 [65]. The computational cost required to run the optimization process in a single 2.4 GHz Intel processor with 4 GB RAM was about 300,000 CPU s, about three and a halfdays. We plan to use parallel computing with a PC cluster in future work; this will considerably reduce the computational time, since each function evaluation can be performed independently.

**Table 1 Effective Mechanical Properties of the Square Unit Cell as a Function of Relative Density**

| | $\rho < 0.3$ | $0.3 < \rho < 1$ |
|---|---|---|
| $\frac{E_1}{E_s} = \frac{E_2}{E_s}$ | $0.58(\rho)^{1.046}$ | $1.27(\rho)^2 - 0.52(\rho) + 0.23$ |
| $\frac{G}{E_s}$ | $0.093(\rho)^{3.07}$ | $1.26(\rho)^3 - 1.33(\rho)^2 + 0.51(\rho) - 0.065$ |
| $\frac{\nu_{21}}{\nu_s} = \frac{\nu_{12}}{\nu_s}$ | $0.7(\rho)^{1.05}$ | $0.68(\rho)^2 + 0.28(\rho) + 0.06$ |

For each point in the objective function space, the stress recovery procedure is applied to verify whether the stresses are admissible. To apply this procedure, the average macroscopic strain inside each unit cell is found. The position of each unit cell within the implant is obtained after imposing a proper cell tessellation, which in this work has been set to be uniform. The size of the unit cell is selected as small as possible to capture the relative distribution contour with higher resolution. For a relative density of 0.1, the square cell sizes for the cell wall thickness of either 70 or 100 $\mu$m have been selected, respectively, to be 1.36 and 1.8 mm. Once the position of the unit cells has been obtained, $3 \times 3$ Gauss points are assigned to each cell. The values of relative density and macroscopic strain at these points are obtained from the relative density distribution and macroscopic strain field. For Gauss points located outside the implant border, the values are linearly extrapolated from those located at the neighboring points inside the implant domain. Using a Gaussian quadrature integration [66], the average relative density and macroscopic strain of each cell are calculated. The local stress distribution and the yield safety factor of each cell are obtained through the von Mises stress criterion. The procedure is applied to all unit cells of the selected optimal design located on the Pareto frontier and the minimum local safety factor of a cell is specified as design safety factor.

## 4 Results and Discussion

The advantage of multiobjective optimization with a posteriori articulation of preference is that a set of optimum solutions are available without requiring the designer to choose in advance any weighting factors to the objective functions. Once the whole set of Pareto solutions has been determined, the designer has the freedom to select the desired solution based on the importance of bone mass preservation relative to the amount of interface stress. Figure 6 shows all the optimum solutions, i.e., the relative density distribution, for a hip stem implant with graded cellular material. The x axis represents the amount of bone resorption for the implanted hip; on the y axis is the interface failure index. Among the optimal solutions, we examine three representative relative density distributions: the extreme points, A and C, of the Pareto frontier, for which one objective function has importance factor 0 and the other 100%, and a solution B characterized by a 50% weight factor. For each solution, Fig. 6 gives the following performance metrics: bone resorption ($m_r$), interface failure index ($F(\boldsymbol{b})$), maximum interface failure ($f(\sigma)_{\max}$), average porosity of each stem ($\bar{\phi}$), and design safety factor ($SF$) after implementing the stress recovery procedure. The maximum interface failure $f(\sigma)_{\max}$ is included since $F(\boldsymbol{b})$, which quantifies only the overall effect of the implant stiffness on the interface stresses, is not sufficient to provide information on the probability of failure.

As seen from the performance metrics in Fig. 6, the porosity of solutions A, B, and C, is greater than 40%, which is satisfactory

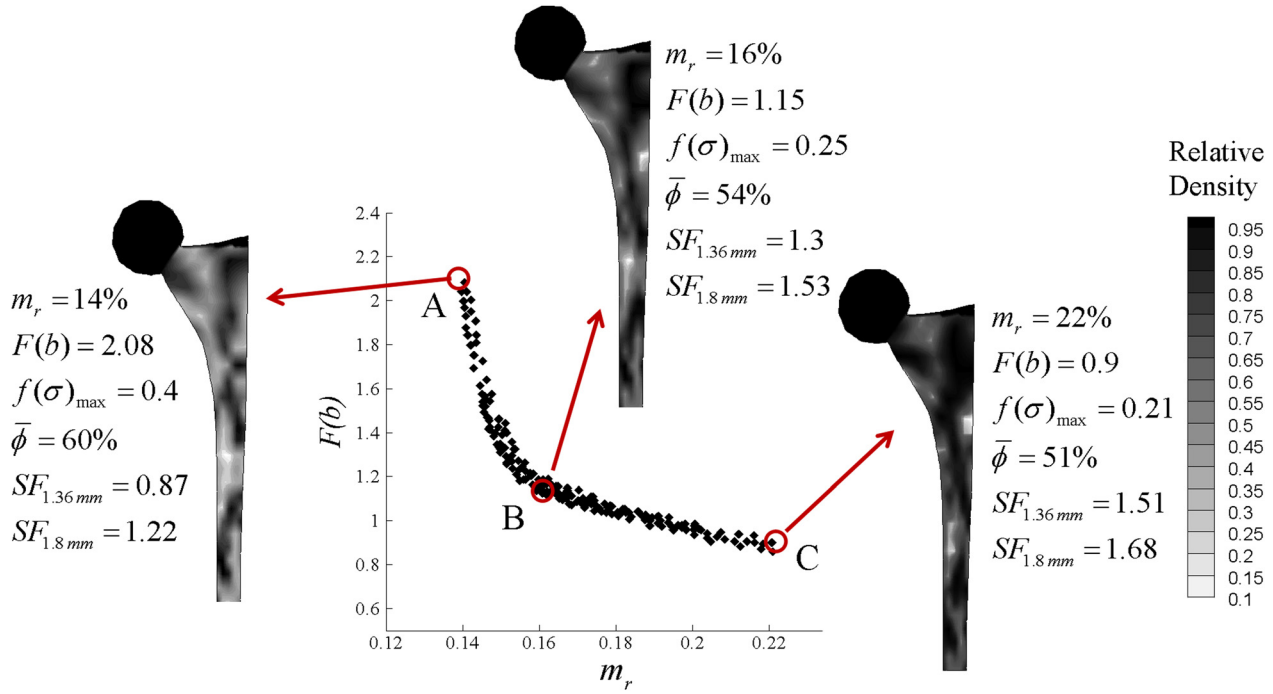


**Fig. 6 Trade-off distributions of relative density for the optimized cellular implant**

for bone ingrowth [41]. By comparing implants C and A, we observe that a raise of the implant porosity from point C to A results in an implant stiffness decrease, which, on one hand, lowers bone loss and, on the other hand, enhances the risk of interface failure. When solution B is compared to C, a reduction of 8% of bone resorption is noted with a slight increase of the peak value of the interface failure. On the other hand, by contrasting solution B to A, we note a significant increase (60%) of the peak value of interface failure, which is below the Hoffman failure strength, and a minor reduction (2%) of the amount of bone resorption. The main benefit of solution A is the maximum porosity of the microstructure that can promote bone ingrowth. Solution B, on the other hand, might be the preferred solution with respect to low bone resorption and interface failure. These observations emerge only by inspection of the objective functions selected in this work; we remark here that other parameters should be taken into account for the selection of the best implant. These include patient's bone characteristics, the range of activity, age, and desired level of bone mass preservation after implantation.

For prescribed geometric loading and constraint conditions, we now compare the metrics of resorbed bone mass ($m_r$) and distribution of interface stress ($f(\sigma^b)$) of the optimal solution B with those of (i) a currently-used fully dense titanium stem and (ii) a cellular implant with a uniformly distributed relative density of 50%. Figures 7 and 8 illustrate the results of the comparison.

For the solid titanium stem, the amount of bone resorption calculated through Eq. (7) is 67%, and the interface failure index $F(\boldsymbol{b})$ obtained from Eq. (8) is 1.33. Using the distribution of $f(\sigma)$ generated around the titanium stem (Fig. 8(*a*)), we observe that the maximum value of interface failure (0.51) occurs at the distal end of the implant. As expected, this implant is much stiffer than the surrounding bone, thereby resulting in a higher amount of bone resorption. For the numerical validation, the interface shear stress of the titanium implant at the proximal region is also

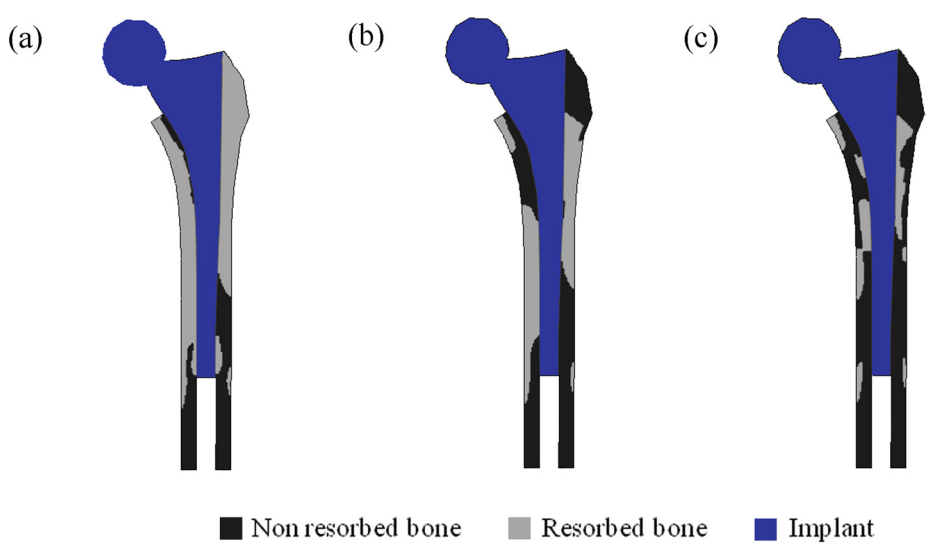


**Fig. 7 Distribution of bone resorption around (*a*) fully dense titanium implant, (*b*) cellular implant with uniform relative density of 50%, (*c*) graded cellular implant (solution B in Fig. 6)**

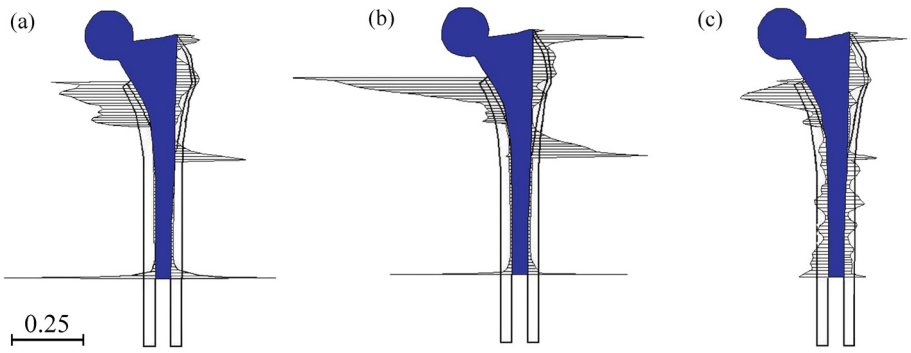


**Fig. 8 Distribution of local interface failure $f(\sigma)$ around (*a*) fully dense titanium implant, (*b*) cellular implant with uniform relative density of 50%, (*c*) graded cellular implant (solution B in Fig. 6)**

compared with the one obtained by Kowalczyk for a 3D model [4]. The mean and the maximum values of interface shear stress for the 3D titanium implant in the work by Kowalczyk [4] are 0.57 and 2.8 MPa, respectively. These values are respectively 0.31 and 2.15 MPa for the titanium implant in this paper. The contribution to the higher level of shear stress in the 3D model of Kowalczyk is the distribution of shear force on a smaller area. In Kowalczyk's study [4], the implant and bone are bonded only at the proximal region, while in our work the whole bone-implant interface is bonded, which results in a decrease of the mean and the maximum values of interface shear stress.

The cellular implant with uniform relative density of 50% is approximately three times more flexible than the titanium stem. This implant can qualitatively simulate the behavior of an implant made out of tantalum foam. For this stem, the amount of bone resorption and the interface failure index are about 34% and 2.87, respectively, and the interface failure is maximum (0.71) at the edge of proximal region. Compared to the solid titanium implant, the amount of bone resorption decreases by 50%, whereas the maximum interface failure increases about 40%. This shows that a decrease of the implant stiffness with uniform porosity distribution aiming at reducing bone resorption has the undesirable effect of increasing the risk of interface failure at the proximal region. This outcome confirms the findings of the previous work by Kuiper and Huiskes [14].

Figure 7(*c*) and 8(*c*) show the results for the graded cellular implant B. Its bone resorption and interface failure index are 16% and 1.15, respectively. The peak value of the local interface failure is 0.25. Compared to the titanium stem, both the amount of bone resorption and the peak of interface failure decrease of 76% and 50%, respectively. With respect to the uniformly-distributed cellular implant, the decrease of bone resorption and interface failure peak is of 53% and 65%, respectively. A graded cellular implant with optimized relative density distribution is thus capable of reducing concurrently both the conflicting objective functions. In particular, bone resorption reduces as a result of the cellular material which makes the implant more compliant; the interface stress, on the other hand, is minimized by the optimized gradients of cellular material.

A proof-of-concept implant was built to verify the manufacturability of the optimum grade lattice material. Figure 9 shows the polypropylene prototype of solution B, which was manufactured with a 3D printer Objet Connex500 [67]. A uniform tessellation and a square unit cell of 1.8 mm size were assumed to draw the model. The cell geometry was calculated from the average relative density obtained from the method described in this paper. An STL file of the graded cellular implant, solution B, was finally used for rapid prototyping.

The limitations of the method proposed in this paper are here discussed. First, the method tackles the design of an implant statically loaded in the stance phase of walking. Further research is required to extend it to variable loading and fatigue life design.


**Fig. 9 Polypropylene proof-of-concept of the optimal graded cellular implant (solution B)**

Second, the accuracy of the asymptotic homogenization needs to be investigated at the vicinity of the implant borders. Although macroscopic mean stress fields on the boundaries are satisfied in the global solutions [40,68], microscopic stresses do not satisfy the *Y*-periodicity assumption. These boundary effects, however, may be captured by applying a boundary layer corrector [68,69], a spatially decaying stress localization function [70], or an adaptive multiscale methodology [71]. To investigate the accuracy of these techniques, it is required to construct a detailed finite element model and compare the actual stress/strain distribution inside the cell walls with the microscopic stresses/strains estimated from the homogenization method. This task will be performed in future.

Third, to extend the proposed procedure to three dimensions, a 3D cell topology with high porosity, interconnected pore structure, large surface area with suitable textures, and good

mechanical properties should be selected [72,73]. The asymptotic homogenization will be applied to characterize tissue scaffolding cell topologies for a wide range of relative density. Their effective moduli, yield and ultimate surfaces for multiaxial loading conditions will be obtained to create a standard library from which to select suitable cell geometries for a 3D cellular implant design.

Fourth, bone has been here considered as consisting of a cancellous and a cortical part with isotropic mechanical properties. Further study is necessary to improve the constitutive material model of bone and to consider bone as a graded cellular material.

Finally in the optimization procedure, a simple formulation has been used to quantitatively measure both bone resorption and implant stability. In a future study, detailed simulations of implant stability [74–77] and bone remodeling process [60,77–80] can be performed to assess both the short and long term performance of the implant.

## 5 Concluding Remarks

This work has presented a methodology integrating multiscale analysis and design optimization to design a novel hip implant made of graded cellular material. The method can contribute to the development of a new generation of orthopedic implants with a graded cellular microstructure that will reduce the clinical consequences of current implants.

In the first part of the paper, the homogenization method has been reviewed and then used to capture the mechanics of the implant at the micro and macro scale. In the second part, multiobjective optimization has been applied to find optimum gradients of material distribution that minimize concurrently bone resorption and bone-implant interface stresses. The results have shown that the optimized cellular implant exhibits a reduction of 76% of bone resorption and 50% of interface stress, with respect to a fully dense titanium implant.

## References


[1] Kurtz, S., Ong, K., Lau, E., Mowat, F., and Halpern, M., 2007, "Projections of Primary and Revision Hip and Knee Arthroplasty in the United States from 2005 to 2030," J. Bone Jt. Surg., Am. Vol., **89**(4), pp. 780–785.

[2] Vichinsky, E. P., Neumayr, L. D., Haberkern, C., Earles, A. N., Eckman, J., Koshy, M., and Black, D. M., 1999, "The Perioperative Complication Rate of Orthopedic Surgery in Sickle Cell Disease: Report of the National Sickle Cell Surgery Study Group," Am. J. Hematol., **62**(3), pp. 129–138.

[3] Kobayashi, S., Saito, N., Horiuchi, H., Iorio, R., and Takaoka, K., 2000, "Poor Bone Quality or Hip Structure as Risk Factors Affecting Survival of Total-Hip Arthroplasty," The Lancet, **355**(9214), pp. 1499–1504.

[4] Kowalczyk, P., 2001, "Design Optimization of Cementless Femoral Hip Prostheses Using Finite Element Analysis," J. Biomech. Eng., **123**(5), pp. 396–402.

[5] Moen, T. C., Ghate, R., Salaz, N., Ghodasra, J., and Stulberg, S. D., 2011, "A Monoblock Porous Tantalum Acetabular Cup Has No Osteolysis on Ct at 10 Years," Clin. Orthop. Relat. Res., **469**(2), pp. 382–386.

[6] Kurtz, S., Gawel, H., and Patel, J., 2011, "History and Systematic Review of Wear and Osteolysis Outcomes for First-Generation Highly Crosslinked Polyethylene," Clin. Orthop. Relat. Res., **469**(8), pp. 2262–2277.

[7] Grübl, A., Marker, M., Brodner, W., Giurea, A., Heinze, G., Meisinger, V., Zehetgruber, H., and Kotz, R., 2007, "Long Term Follow up of Metal on Metal Total Hip Replacement," J. Orthop. Res., **25**(7), pp. 841–848.

[8] Neumann, D. R. P., Thaler, C., Hitzl, W., Huber, M., Hofstädter, T., and Dorn, U., 2010, "Long-Term Results of a Contemporary Metal-on-Metal Total Hip Arthroplasty: A 10-Year Follow-up Study," J. Arthroplasty, **25**(5), pp. 700–708.

[9] Glassman, A., Bobyn, J., and Tanzer, M., 2006, "New Femoral Designs Do They Influence Stress Shielding?," Clin. Orthop. Relat. Res., **453**(12), pp. 64–74.

[10] Adam, F., Hammer, D. S., Pfautsch, S., and Westermann, K., 2002, "Early Failure of a Press-Fit Carbon Fiber Hip Prosthesis with a Smooth Surface," J. Antroplasty, **17**(2), pp. 217–223.

[11] Trebse, R., Milosev, I., Kovac, S., Mikek, M., and Pisot, V., 2005, "Poor Results from the Isoelastic Total Hip Replacement," Acta Orthop., **76**(2), pp. 169–176.

[12] Harvey, E., Bobyn, J., Tanzer, M., Stackpool, G., Krygier, J., and Hacking, S., 1999, "Effect of Flexibility of the Femoral Stem on Bone-Remodeling and Fixation of the Stem in a Canine Total Hip Arthroplasty Model without Cement," J. Bone Jt. Surg., **81**(1), pp. 93–107.

[13] Huiskes, R., Weinans, H., and Rietbergen, B., 1992, "The Relationship between Stress Shielding and Bone Resorption around Total Hip Stems and the Effects of Flexible Materials," Clin. Orthop. Relat. Res., **274**(1), pp. 124–134.

[14] Kuiper, J., and Huiskes, R., 1992, "Numerical Optimization of Hip-Prosthetic Stem Material," *Recent Advances in Computer Methods in Biomechanics and Biomedical Engineering*, J. Middleton, G. N. Pande, and K. R. Williams, eds., Books and Journals International Ltd., Swansea, pp. 76–84.

[15] Kuiper, J. H., and Huiskes, R., 1997, "Mathematical Optimization of Elastic Properties: Application to Cementless Hip Stem Design," J. Biomech. Eng., **119**(2), pp. 166–174.

[16] Hedia, H., Shabara, M., El-Midany, T., and Fouda, N., 2006, "Improved Design of Cementless Hip Stems Using Two-Dimensional Functionally Graded Materials," J. Biomed. Mater. Res., Part B: Appl. Biomater., **79**(1), pp. 42–49.

[17] Hedia, H. S., and Mahmoud, N.-A., 2004, "Design Optimization of Functionally Graded Dental Implant," Biomed. Mater. Eng., **14**(2), pp. 133–143.

[18] Watari, F., Yokoyama, A., Saso, F., Uo, M., and Kawasaki, T., 1997, "Fabrication and Properties of Functionally Graded Dental Implant," Composites, Part B, **28**(1-2), pp. 5–11.

[19] Katti, K. S., 2004, "Biomaterials in Total Joint Replacement," Colloids Surf., B **39**(3), pp. 133–142.

[20] Thompson, I., and Hench, L., 1998, "Mechanical Properties of Bioactive Glasses, Glass-Ceramics and Composites," Proc. Inst. Mech. Eng., Part H: J. Eng. Med., **212**(2), pp. 127.

[21] Fraldi, M., Esposito, L., Perrella, G., Cutolo, A., and Cowin, S., 2010, "Topological Optimization in Hip Prosthesis Design," Biomech. Model. Mechanobiol., **9**(4), pp. 389–402.

[22] Bobyn, J. D., Poggie, R., Krygier, J., Lewallen, D., Hanssen, A., Lewis, R., Unger, A., O'keefe, T., Christie, M., and Nasser, S., 2004, "Clinical Validation of a Structural Porous Tantalum Biomaterial for Adult Reconstruction," J. Bone Jt. Surg., **86**(Supplement 2), pp. 123–129.

[23] Bobyn, J., Stackpool, G., Hacking, S., Tanzer, M., and Krygier, J., 1999, "Characteristics of Bone Ingrowth and Interface Mechanics of a New Porous Tantalum Biomaterial," J. Bone Jt. Surg., Br. Vol., **81**(5), pp. 907–914.

[24] Parthasarathy, J., Starly, B., Raman, S., and Christensen, A., 2010, "Mechanical Evaluation of Porous Titanium (Ti6al4v) Structures with Electron Beam Melting (Ebm)," J. Mech. Behav. Biomed. Mater., **3**(3), pp. 249–259.

[25] Heinl, P., Müller, L., Körner, C., Singer, R. F., and Müller, F. A., 2008, "Cellular Ti-6al-4v Structures with Interconnected Macro Porosity for Bone Implants Fabricated by Selective Electron Beam Melting," Acta Biomater., **4**(5), pp. 1536–1544.

[26] Stamp, R., Fox, P., O'neill, W., Jones, E., and Sutcliffe, C., 2009, "The Development of a Scanning Strategy for the Manufacture of Porous Biomaterials by Selective Laser Melting," J. Mater. Sci.: Mater. Med., **20**(9), pp. 1839–1848.

[27] Yang, S., Leong, K., Du, Z., and Chua, C., 2002, "The Design of Scaffolds for Use in Tissue Engineering. Part Ii. Rapid Prototyping Techniques," Tissue Eng., **8**(1), pp. 1–11.

[28] Murr, L., Gaytan, S., Medina, F., Lopez, H., Martinez, E., Machado, B., Hernandez, D., Martinez, L., Lopez, M., and Wicker, R., 2010, "Next-Generation Biomedical Implants Using Additive Manufacturing of Complex, Cellular and Functional Mesh Arrays," Philos. Trans. R. Soc. London, Ser. A, **368**(1917), pp. 1999–2032.

[29] Coelho, P., Fernandes, P., Guedes, J., and Rodrigues, H., 2008, "A Hierarchical Model for Concurrent Material and Topology Optimisation of Three-Dimensional Structures," Struct. Multidiscip. Optim., **35**(2), pp. 107–115.

[30] Rodrigues, H., Guedes, J., and Bendsoe, M., 2002, "Hierarchical Optimization of Material and Structure," Struct. Multidiscip. Optim., **24**(1), pp. 1–10.

[31] Gonçalves Coelho, P., Rui Fernandes, P., and Carriço Rodrigues, H., 2011, "Multiscale Modeling of Bone Tissue with Surface and Permeability Control," J. Biomech., **44**(2), pp. 321–329.

[32] Coelho, P. G., Cardoso, J. B., Fernandes, P. R., and Rodrigues, H. C., 2011, "Parallel Computing Techniques Applied to the Simultaneous Design of Structure and Material," Adv. Eng. Software, **42**(5), pp. 219–227.

[33] Gibson, L. J., and Ashby, M. F., 1999, *Cellular Solids: Structure and Properties*, Cambridge University Press, Cambridge, UK.

[34] Guedes, J., and Kikuchi, N., 1990, "Preprocessing and Postprocessing for Materials Based on the Homogenization Method with Adaptive Finite Element Methods," Comput. Methods Appl. Mech. Eng., **83**(2), pp. 143–198.

[35] Hassani, B., and Hinton, E., 1998, "A Review of Homogenization and Topology Optimization I-Homogenization Theory for Media with Periodic Structure," Comput. Struct., **69**(6), pp. 707–717.

[36] Hassani, B., and Hinton, E., 1998, "A Review of Homogenization and Topology Opimization I I-Analytical and Numerical Solution of Homogenization Equations," Comput. Struct., **69**(6), pp. 719–738.

[37] Fang, Z., Starly, B., and Sun, W., 2005, "Computer-Aided Characterization for Effective Mechanical Properties of Porous Tissue Scaffolds," Comput.-Aided Des., **37**(1), pp. 65–72.

[38] Zienkiewicz, O. C., and Taylor, R. L., 2005, *The Finite Element Method for Solid and Structural Mechanics*, 6th ed., Butterworth-Heinemann, Burlington.

[39] Hollister, S., and Kikuchi, N., 1992, "A Comparison of Homogenization and Standard Mechanics Analyses for Periodic Porous Composites," Comput. Mech., **10**(2), pp. 73–95.

[40] Pellegrino, C., Galvanetto, U., and Schrefler, B., 1999, "Numerical Homogenization of Periodic Composite Materials with Non Linear Material Components," Int. J. Numer. Methods Eng., **46**(10), pp. 1609–1637.

[41] Bragdon, C., Jasty, M., Greene, M., Rubash, H., and Harris, W., 2004, "Biologic Fixation of Total Hip Implants: Insights Gained from a Series of Canine Studies," J. Bone Jt. Surg., **86**(Supplement 2), pp. 105–117.

[42] Harrysson, O. L. A., Cansizoglu, O., Marcellin-Little, D. J., Cormier, D. R., and West Ii, H. A., 2008, "Direct Metal Fabrication of Titanium Implants with Tailored Materials and Mechanical Properties Using Electron Beam Melting Technology," Mater. Sci. Eng. C, **28**(3), pp. 366–373.

[43] Wang, H. V., 2005, "A Unit Cell Approach for Lightweight Structure and Compliant Mechanism," Ph.D. thesis, Georgia Institute Of Technology, Atlanta, GA.
[44] Matsui, K., Terada, K., and Yuge, K., 2004, "Two-Scale Finite Element Analysis of Heterogeneous Solids with Periodic Microstructures," Comput. Struct., **82**(7-8), pp. 593–606.
[45] Masters, I., and Evans, K., 1996, "Models for the Elastic Deformation of Honeycombs," Compos. Struct., **35**(4), pp. 403–422.
[46] Christensen, R. M., 2000, "Mechanics of Cellular and Other Low-Density Materials," Int. J. Solids Struct., **37**(1-2), pp. 93–104.
[47] Wang, A., and Mcdowell, D., 2004, "In-Plane Stiffness and Yield Strength of Periodic Metal Honeycombs," J. Eng. Mater. Technol., **126**(2), pp. 137–156.
[48] Kumar, R., and Mcdowell, D., 2004, "Generalized Continuum Modeling of 2-D Periodic Cellular Solids," Int. J. Solids Struct., **41**(26), pp. 7399–7422.
[49] Warren, W., and Byskov, E., 2002, "Three-Fold Symmetry Restrictions on Two-Dimensional Micropolar Materials," Eur. J. Mech. A/Solids, **21**(5), pp. 779–792.
[50] Chen, J., and Huang, M., 1998, "Fracture Analysis of Cellular Materials: A Strain Gradient Model," J. Mech. Phys. Solids, **46**(5), pp. 789–828.
[51] Wang, W.-X., Luo, D., Takao, Y., and Kakimoto, K., 2006, "New Solution Method for Homogenization Analysis and Its Application to the Prediction of Macroscopic Elastic Constants of Materials with Periodic Microstructures," Comput. Struct., **84**(15-16), pp. 991–1001.
[52] Andrews, E., Gioux, G., Onck, P., and Gibson, L., 2001, "Size Effects in Ductile Cellular Solids. Part II: Experimental Results," Int. J. Mech. Sci., **43**(3), pp. 701–713.
[53] Simone, A., and Gibson, L., 1998, "Effects of Solid Distribution on the Stiffness and Strength of Metallic Foams," Acta Mater., **46**(6), pp. 2139–2150.
[54] Bendsøe, M. P., and Sigmund, O., 2003, *Topology Optimization: Theory, Methods, and Applications*, Springer-Verlag, Berlin.
[55] Hassani, B., and Hinton, E., 1998, "A Review of Homogenization and Topology Optimization III-Topology Optimization Using Optimality Criteria," Comput. Struct., **69**(6), pp. 739–756.
[56] Díaaz, A., and Kikuchi, N., 1992, "Solutions to Shape and Topology Eigenvalue Optimization Problems Using a Homogenization Method," Int. J. Numer. Methods Eng., **35**(7), pp. 1487–1502.
[57] Suzuki, K., and Kikuchi, N., 1991, "A Homogenization Method for Shape and Topology Optimization," Comput. Methods Appl. Mech. Eng., **93**(3), pp. 291–318.
[58] Bendsøe, M. P., and Kikuchi, N., 1988, "Generating Optimal Topologies in Structural Design Using a Homogenization Method," Comput. Methods Appl. Mech. Eng., **71**(2), pp. 197–224.
[59] Hassani, B., 1996, "A Direct Method to Derive the Boundary Conditions of the Homogenization Equation for Symmetric Cells," Commun. Numer. Methods Eng., **12**(3), pp. 185–196.
[60] Weinans, H., Huiskes, R., and Grootenboer, H., 1992, "Effects of Material Properties of Femoral Hip Components on Bone Remodeling," J. Orthop. Res., **10**(6), pp. 845–853.
[61] Hoffman, O., 1967, "The Brittle Strength of Orthotropic Material," J. Compos. Mater., **1**(3), pp. 200–206.
[62] Pal, B., Gupta, S., and New, A., 2009, "A Numerical Study of Failure Mechanisms in the Cemented Resurfaced Femur: Effects of Interface Characteristics and Bone Remodelling," Proc. Inst. Mech. Eng., Part H: J. Eng. Med., **223**(4), pp. 471–484.
[63] Carter, D., Orr, T., and Fyhrie, D., 1989, "Relationships between Loading History and Femoral Cancellous Bone Architecture," J. Biomech., **22**(3), pp. 231–244.
[64] Bidanda, B., and Bártolo, P., 2008, *Virtual Prototyping & Bio Manufacturing in Medical Applications*, Springer-Verlag, Berlin, Chap. 5.
[65] Deb, K., Pratap, A., Agarwal, S., and Meyarivan, T., 2002, "A Fast and Elitist Multiobjective Genetic Algorithm: Nsga-Ii," IEEE Trans. Evol. Comput., **6**(2), pp. 182–197.
[66] Zienkiewicz, O. C., and Taylor, R. L., 2005, *The Finite Element Method for Solid and Structural Mechanics*, Butterworth-Heinemann, Burlington.
[67] Objet-Geometries, I., 2011, http:/www.objet.com/
[68] Lefik, M., and Schrefler, B., 1996, "FE Modelling of a Boundary Layer Corrector for Composites Using the Homogenization Theory," Eng. Comput., **13**(6), pp. 31–42.
[69] Dumontet, H., 1986, "Study of a Boundary Layer Problem in Elastic Composite Materials," RAIRO Model. Math. Anal. Numer, **20**(2), pp. 265–286.
[70] Kruch, S., 2007, "Homogenized and Relocalized Mechanical Fields," J. Strain Anal. Eng. Des., **42**(4), pp. 215–226.
[71] Ghosh, S., Lee, K., and Raghavan, P., 2001, "A Multi-Level Computational Model for Multi-Scale Damage Analysis in Composite and Porous Materials," Int. J. Solids Struct., **38**(14), pp. 2335–2385.
[72] Cheah, C., Chua, C., Leong, K., and Chua, S., 2003, "Development of a Tissue Engineering Scaffold Structure Library for Rapid Prototyping. Part 2: Parametric Library and Assembly Program," Int. J. Adv. Manuf. Technol., **21**(4), pp. 302–312.
[73] Cheah, C., Chua, C., Leong, K., and Chua, S., 2003, "Development of a Tissue Engineering Scaffold Structure Library for Rapid Prototyping. Part 1: Investigation and Classification," Int. J. Adv. Manuf. Technol., **21**(4), pp. 291–301.
[74] Viceconti, M., Monti, L., Muccini, R., Bernakiewicz, M., and Toni, A., 2001, "Even a Thin Layer of Soft Tissue May Compromise the Primary Stability of Cementless Hip Stems," Clin. Biomech., **16**(9), pp. 765–775.
[75] Viceconti, M., Brusi, G., Pancanti, A., and Cristofolini, L., 2006, "Primary Stability of an Anatomical Cementless Hip Stem: A Statistical Analysis," J. Biomech., **39**(7), pp. 1169–1179.
[76] Abdul-Kadir, M. R., Hansen, U., Klabunde, R., Lucas, D., and Amis, A., 2008, "Finite Element Modelling of Primary Hip Stem Stability: The Effect of Interference Fit," J. Biomech., **41**(3), pp. 587–594.
[77] Viceconti, M., Muccini, R., Bernakiewicz, M., Baleani, M., and Cristofolini, L., 2000, "Large-Sliding Contact Elements Accurately Predict Levels of Bone-Implant Micromotion Relevant to Osseointegration," J. Biomech., **33**(12), pp. 1611–1618.
[78] Weinans, H., Huiskes, R., and Grootenboer, H. J., 1992, "The Behavior of Adaptive Bone-Remodeling Simulation Models," J. Biomech., **25**(12), pp. 1425–1441.
[79] Boyle, C., and Kim, I. Y., 2011, "Three-Dimensional Micro-Level Computational Study of Wolff's Law Via Trabecular Bone Remodeling in the Human Proximal Femur Using Design Space Topology Optimization," J. Biomech., **44**(5), pp. 935–942.
[80] Boyle, C., and Kim, I. Y., 2011, "Comparison of Different Hip Prosthesis Shapes Considering Micro-Level Bone Remodeling and Stress-Shielding Criteria Using Three-Dimensional Design Space Topology Optimization," J. Biomech., **44**(9), pp. 1722–1728.